

Ripple structure of crystalline layers in ion-beam-induced Si wafers

S. Hazra, T. K. Chini, and M. K. Sanyal

Surface Physics Division, Saha Institute of Nuclear Physics, 1/AF Bidhannagar, Kolkata 700 064, India

J. Grenzer and U. Pietsch

Institut für Physik, Universität Potsdam, 14415 Potsdam, Germany

(Received 12 May 2004; revised manuscript received 16 July 2004; published 27 September 2004)

Ion-beam-induced ripple formation in Si wafers was studied by two complementary surface sensitive techniques, namely atomic force microscopy (AFM) and depth-resolved x-ray grazing incidence diffraction (GID). The formation of ripple structure at high doses ($\sim 7 \times 10^{17}$ ions/cm²), starting from initiation at low doses ($\sim 1 \times 10^{17}$ ions/cm²) of ion beam, is evident from AFM, while that in the buried crystalline region below a partially crystalline top layer is evident from GID study. Such ripple structure of crystalline layers in a large area formed in the subsurface region of Si wafers is probed through a nondestructive technique. The GID technique reveals that these periodically modulated wavelike buried crystalline features become highly regular and strongly correlated as one increases the Ar ion-beam energy from 60 to 100 keV. The vertical density profile obtained from the analysis of a Vineyard profile shows that the density in the upper top part of ripples is decreased to about 15% of the crystalline density. The partially crystalline top layer at low dose transforms to a completely amorphous layer for high doses, and the top morphology was found to be conformal with the underlying crystalline ripple.

DOI: 10.1103/PhysRevB.70.121307

PACS number(s): 81.16.Rf, 61.10.Nz, 68.37.Ps, 68.35.Fx

The formation of periodic ripple or a wavelike pattern with a spatial periodicity varying from nm to μm range on obliquely ion-bombarded solid surfaces has become a topic of intense research in the context of fabrication of nanoscale textured materials,¹ such as templates for growing nanowire, nanorods, or nanodots. Ion-induced ripples are thought to be produced by interplay between a roughening process caused by the ion-beam erosion (sputtering) of surface and a smoothing process caused by thermal or ion-induced surface diffusion.^{2–4} The balance between positive surface diffusion and negative surface tension develops instability along the projection of the ion beam and also perpendicular to it, leading to ripple formation in both directions. However, experimentally observed ripple structure has the direction for which the growth rate is largest and is generally along the projection of the ion beam, consistent with current theoretical models.^{1–3}

It is an established fact that monocrystalline semiconductors may be rendered amorphous, easily compared to crystalline metals under room-temperature keV energy heavy-ion (such as Ar) impact.⁵ However, our conventional wisdom on ion-solid interaction does not answer the question whether the amorphous/crystalline interface underneath the top surface maintains its planarity when the semiconductor surface under oblique ion bombardment transforms its initial flat geometry to a corrugated one. This is a relevant question in accounting for the extent of the disordered zone responsible in the smoothing mechanism by viscous relaxation assumed in some recent models⁶ of ripple formation in semiconductors. Interestingly, quite recently,⁷ a cross-sectional transmission electron microscopy (XTEM) study on an obliquely incident (50–120) keV Ar⁺ bombarded Si surface showed that the crystalline part at the buried amorphous crystalline interface also follows the same sinusoidal ripple pattern as formed in the top amorphous layer. The Ar⁺ dose employed in this study was about 10^{18} ions/cm², an order of

magnitude higher than the critical dose (10^{17} ions/cm²) for ripple formation under similar experimental conditions. Although XTEM can provide unique information about out-of-plane interfacial structure, it cannot give the information about in-plane interfacial structure that is essential to understand the process of ripple evolution for the Ar-Si combination through the study of top as well as buried damaged layer in the dose range between 10^{17} and 10^{18} ions/cm² (i.e., from the period of ripple initiation to a stage of full grown ripple).

Surface sensitive x-ray scattering is an extremely powerful technique to probe the surface and buried interfaces of a system in a nondestructive and statistical way.^{8–11} In particular, grazing incidence diffraction (GID) is sensitive to the in-plane crystalline structure^{12–16} and can be used to map the in-plane structure as a function of depth. The purpose of the present work is to demonstrate how GID can be utilized to bring out the subsurface (amorphous-crystalline interface) ripple structure in addition to the top ripple structure observed by atomic force microscopy (AFM) of a keV ion-beam-modified Si(001) surface.

In these experiments, small pieces (20 mm \times 10 mm) of samples cut from a one-sided mirror polished Si(001) wafer were bombarded with focused (typical beam spot of 1.5 mm \times 2.5 mm) ⁴⁰Ar⁺ beam delivered from a 200-keV high current ion implanter (Danfysik).³ The ion-beam incidence angle (Ψ) was kept at 60°, while the energy (E) and dose (ϕ) of the bombarded ions varied in the range of 60–100 keV and $(1–7) \times 10^{17}$ ions/cm², respectively. To obtain homogeneous irradiation, the focused ion beam was scanned with a magnetic x - y sweeping system and passed through a circular aperture (diameter of 4 mm) that defined an elliptical beam spot on the sample. The vacuum in the implantation chamber during irradiation remained in the 10^{-7} mbar region.

The top surface morphology of the ion-bombarded Si(001) samples was studied using atomic force microscope

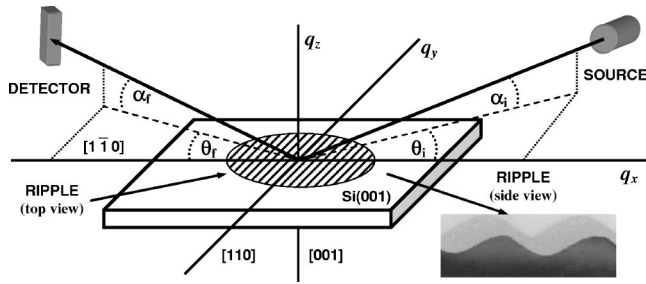


FIG. 1. Schematic of the scattering geometry used to perform GID measurements of patterned structure. The inset shows the side view of the sample as obtained from XTEM.⁷ Details are given in the text.

(AutoProbe CP, PSI) in constant force mode.¹⁷ Each sample was scanned for a different scan size and in a different region to get the statistically averaged information. The underlying or subsurface structures of the same ion-beam modified Si samples were estimated by performing GID measurements¹³ using a synchrotron source [European Synchrotron Radiation Facility (ESRF) ID01 beam line] of beam size $0.2 \times 0.2 \text{ mm}^2$ and wavelength $\lambda = 1.55 \text{ \AA}$. The scattering geometry for x-ray measurements is shown in Fig. 1. The components of the wave vector (q) is given by $q_x = k_0(\cos \alpha_f \cos \theta_f - \cos \alpha_i \cos \theta_i)$, $q_y = k_0(\cos \alpha_f \sin \theta_f + \cos \alpha_i \sin \theta_i)$, and $q_z = k_0(\sin \alpha_f + \sin \alpha_i)$, where $k_0 = 2\pi/\lambda$; $\alpha_{i,f}$ and $\theta_{i,f}$ are the in-plane and out-of-plane angles, respectively, as shown in Fig. 1. In the materials, q_z , however, becomes $q_z' = 2k_0(\sin^2 \alpha_f - \sin^2 \alpha_c - i4\mu/k_0)^{1/2}$, where α_c is the critical angle which is proportional to the square root of the material density, and μ is the absorption coefficient of the materials. For perfect Si, $\alpha_c \approx 0.23^\circ$ and $\mu \approx 1.44 \times 10^{-6} \text{ \AA}^{-1}$. Also, we used the condition $\alpha_f = \alpha_i$, as done in all measurements. The data has been collected by rocking the sample in plane (i.e., $\theta_i + \theta_f = 2\theta_B$) around the (220) Bragg angle (θ_B) of the Si wafer. We have placed the sample in such a way that this is equivalent to scan the samples along the q_x direction, which is the $[1 \bar{1} 0]$ crystallographic direction of the Si wafer and also the wave direction of the top ripplelike structure. To exploit the effect of the penetration depth, $\Lambda = 1/\text{Im}(q_z')$, the same set of data has been collected by changing α_i . The vertical depth profile was probed by recording Vineyard profiles,¹⁸ where α_i was varied for fixed q_x .

Typical AFM images for ion-beam modified Si surfaces and corresponding GID curves are shown in Fig. 2. Ripple-like structure is evident in all AFM images and is also clear in the typical line profile (inset of Fig. 2) drawn horizontally through each image. The period of such ripple, known as ripple wavelength, is calculated by counting the ripple per unit length. Since this ripple is primarily due to the modulation of amorphous layers, we designated this wavelength as λ_a . The average value of λ_a is then estimated by considering scans of different size and in different portions of a particular sample, which is tabulated in Table I for different E . It is evident from Fig. 2, as well as from the table, that the ripple wavelength increases as we increase E from 60 to 100 keV for a fixed dose, consistent with our earlier observation.³

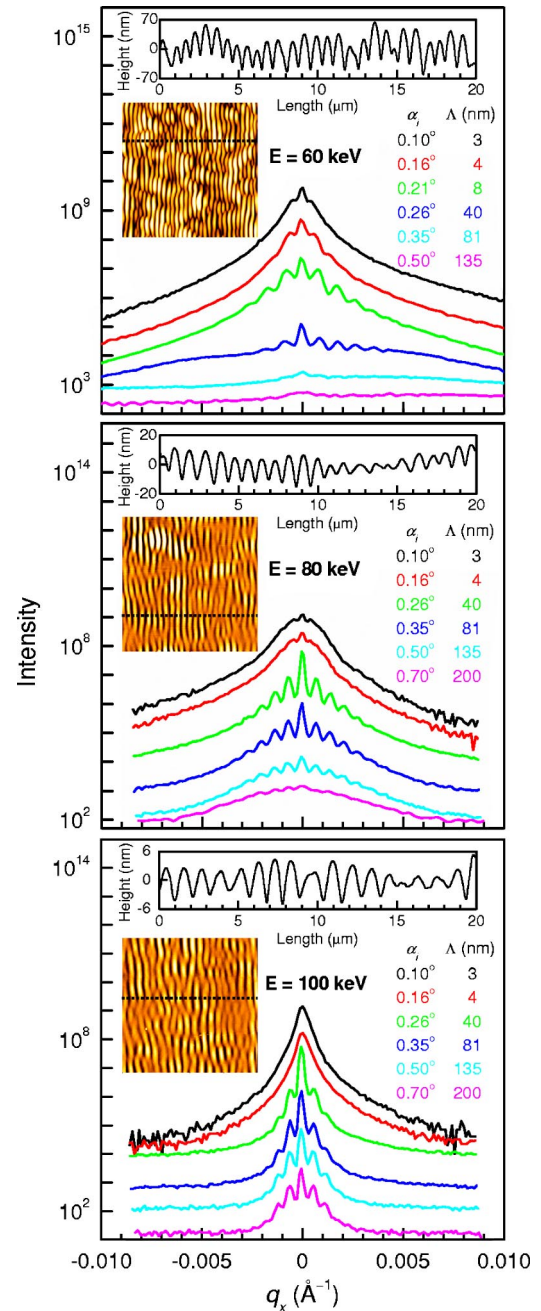


FIG. 2. (Color online) Transverse GID curves around (220) Bragg peak of Si(001) for a different angle of incidence (α_i), i.e., x-ray penetration depth (Λ) in three panels for three Si wafers modified by Ar^+ ion beam for fixed dose $\phi = 7 \times 10^{17} \text{ ions/cm}^2$, but for different energies. In each panel, curves are shifted vertically for clarity. Insets: corresponding typical AFM image (of scan size $20 \mu\text{m} \times 20 \mu\text{m}$) and line profile drawn horizontally (dashed line) through the AFM image, indicative of typical height variation in each sample.

The GID q_x curves for the ion-bombarded samples (Fig. 2) show the presence of satellite peaks on both sides of the main (220) Bragg peak. It is well known that the appearance of a Bragg peak in GID geometry requires the existence of a crystalline lattice structure. Also, the appearance of satellite peaks must be originated by a lateral undulation of the crys-

TABLE I. Ripple wavelength estimated using two complementary techniques, namely AFM and GID.

Technique	Ripple wavelength λ (nm) for E		
	60 keV	80 keV	100 keV
AFM (λ_a)	700 \pm 30	890 \pm 40	1,050 \pm 60
GID (λ_c)	720 \pm 20	915 \pm 15	1,080 \pm 20

talline part of the sample. As seen in Fig. 2, the presence of satellite peaks in q_x scans is prominent after certain values of α_i , which indicates that the ripplelike modulation of crystalline materials is prominent below a certain depth from the top surface. Values of Λ corresponding to the value of α_i are indicated in Fig. 2. It can be noted that the value mentioned in Fig. 2 has been calculated considering the values of α_c and μ for perfect Si. As the top portion of the Si wafer gets modified (density decreased) due to ion bombardment, the value of Λ will be more than that indicated in Fig. 2. For very low α_i no satellite peaks were found, which indicates the absence of lateral correlation of the material in the top layer. However, a distinct but broad Bragg peak can be observed, indicating the existence of remaining crystalline material. With increasing α_i the number of grating peaks increases, reflecting the increasing correlation of ripples in the crystalline material. At a certain value of $\alpha_i \approx \alpha_m$ the shape of the curve changes from a narrow to a broad one, indicating the onset of defect formation. This transition is prominent for the sample with $E=60$ keV and also visible for sample with $E=80$ keV, but not for sample with $E=100$ keV, where this depth might be larger than the maximum Λ probed by GID (about 500 nm). The depth of this transition is obviously related to the penetration depth of the implanted ions, which increases with the increase of E due to a reduced interaction of the implanted ions with the host lattice as predicted from the stopping and range of ions in matter (SRIM) calculation.¹⁹ This finding corresponds to the decrease of ripple height (amplitude) with the increase of E .

The separation between the satellite peaks (Δq_x) observed in the GID curves is inversely proportional to the subsurface ripple wavelength. Unlike ripple on the top surface, the subsurface ripple is made of crystalline layers and the corresponding wavelength is designated by $\lambda_c (=2\pi/\Delta q_x)$. The values of λ_c are determined from the distance between the satellites and are tabulated in Table I. It shows that the value of λ_c increases with E . It can be noted that the values of λ_c agree very well with the corresponding values at the surface, λ_a , which signifies that the growth mechanism of two different ripplelike structures (one on top and another in the subsurface regime) are strongly correlated.

Vineyard profiles for samples bombarded with different dose are shown in Fig. 3. Such α_i scans are very much different from a typical shape, where a single peak at $\alpha_i = \alpha_c$ is observed. Instead, for the present samples, one observed an additional hump (plateau) starting at around $\alpha_i = \alpha_c'$. This corresponds to materials of low but gradually decreasing density on the top. However, since the measurements are on an in-plane Bragg peak, intensities at both α_c and α_c' corre-

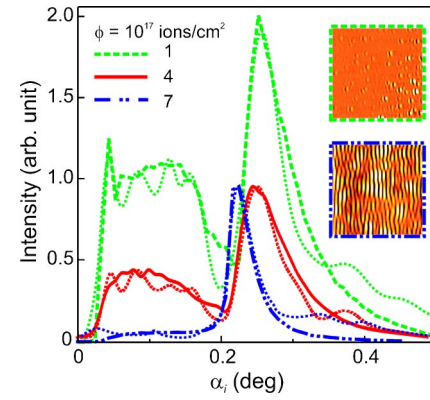


FIG. 3. (Color online) Experimental and simulated (dotted) α_i scans of samples measured at (220) Bragg peak of Si(001) substrate irradiated with different dose at $E=80$ keV. AFM images (of scan size $20 \mu\text{m} \times 20 \mu\text{m}$) of the corresponding low (top) and high (bottom) dose samples are shown in the inset.

spond to the density of crystalline materials. The position of these peaks, and the plateau in between, represent the total density of silicon having dispersed crystallites as a function of depth. It can be noted that the onset angle α_c' , the shape and height of the plateau, and α_c all are functions of implantation dose. For low doses there are two distinct critical angles; the appearance of a peak at $\alpha_c' \approx 0.05^\circ$ corresponds to the existence of a partial crystalline top layer with a much lower density compared to that of crystalline silicon (α_c). The position of α_c appears at a slightly higher angle due to the large roughness of the noncrystalline top layer. For increasing dose the intensity of the plateau region decreases. In case of $\phi = 7 \times 10^{17}$ ions/cm², the plateau region almost disappears and the shape of the α_i scan curve corresponds to a typical Vineyard profile through a dead (amorphous) top layer.¹¹ Thus α_c is not influenced by the amorphous top layer and appears at the correct value.

In order to calculate the vertical density profile we simulated the scattering intensity of a Vineyard profile using the following expression:¹³

$$I(\alpha_i) = |T(\alpha_i)S(q)T(\alpha_j)|^2,$$

using

$$T(\alpha)|_{j \rightarrow j-1} = \frac{t'_{j-1}}{1 + R_{j-1}r'_j} T_j, \quad R(\alpha)|_{j \rightarrow j-1} = \frac{r'_j + R_{j-1}}{1 + R_{j-1}r'_j},$$

$$t'_j = t_j \exp\left[\sigma_{j-1}^2 (q_{z_{j-1}}^2 - q_{z_j}^2)/2\right],$$

$$r'_j = r_j \exp\left[-2\sigma_{j-1}^2 (q_{z_{j-1}} q_{z_j})\right],$$

where $T(\alpha)$ and $R(\alpha)$ are the transmission and reflection functions, respectively. Both functions depend on the transmission, $t(\alpha)$, and reflection, $r(\alpha)$, coefficients which are corrected by an interface-related Debye–Waller factor, σ_j .¹³ $S(q)$ is the structure factor containing the information about the crystalline structure, which was assumed to be a constant function of depth.

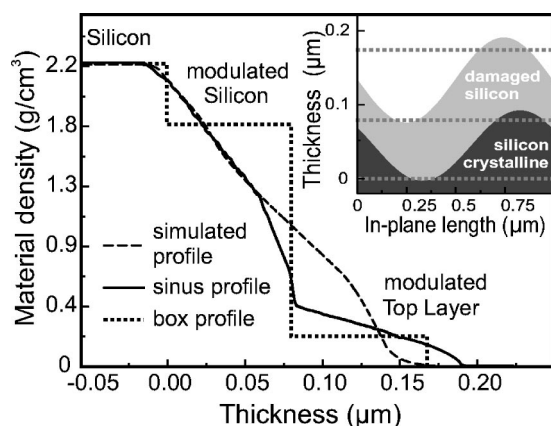


FIG. 4. Reconstructed depth profile of a sample implanted with $\phi = 4 \times 10^{17}$ ions/cm² at $E = 80$ keV. The inset shows the schematic side view of the sample used for the depth profile calculation.

The reconstructed depth profile obtained from the simulation of the Vineyard profile for a sample is shown in Fig. 4. Here, we approximated the varying density of the structure by a three-box model; the first box for crystalline silicon with a density, $\rho_{\text{Si}} \approx 2.2$ g/cm³, the second box for the transition region between the damaged and crystalline material, and the third box for the strongly damaged surface region (see the inset of Fig. 4). Assuming a homogeneous density and an ideal sinusoidal shape of ripples, the projection of the structure onto an axis parallel to the surface normal provides a vertical density profile as shown by the thick line in Fig. 4. This profile becomes modified (broken line) using the box density profile (dotted line), where the box densities were fitted to the measured Vineyard profiles shown in Fig. 3. The strongest deviation from the ideal profile is found for the top box, where the material density is very low, about 15% of ρ_{Si} ; also, the modulated region of the crystalline part is damaged and has a reduced density. A similar simulation was

made for other samples bombarded with different doses, which shows that for low doses, although the top layer density is low, it is still partially crystalline, while the buried layer is almost perfect. With the increase of dose, the top layer becomes more amorphous and the buried layer starts modulating, which decreases the crystalline density. The low density of the top layer is also evident from the contrast of the XTEM image⁷ shown in the inset of Fig. 1, which is essentially arising due to the presence of defects, voids, and Ar bubbles in large amounts. Amorphization of Si by heavy-ion (such as Ar) bombardment at keV energies occurs in a dose range $\sim 10^{14}$ ions/cm² that is much lower than the required dose ($\sim 10^{17}$ ions/cm²) for ripples just to appear as in the present experiment. However, based on the grazing incidence x-ray scattering technique, the presence of a remaining crystalline structure on the top portion of the silicon sample bombarded with off-normal Ar ions of dose 10^{17} ions/cm² is surprising.

In conclusion, the formation of ripplelike structure of crystalline materials is evident in the subsurface region of the Si wafer due to ion bombardment. Such structure, prominent at a certain depth, depends on both the energy and dose of the ion beam. The wavelength of the underlying ripple structure resembles well that of the top surface. The number of created defects increases with the implantation dose, which creates a highly damaged top region. This region retains crystalline nature for low doses but changes to amorphous for higher doses. The buried ripple structure of crystalline silicon, having apparently better regularity than the top amorphous morphology, observed here, will help us to link the ion-solid interaction processes responsible in the formation of nanostructures in metal and semiconductor surfaces.

We would like to thank H. Metzger for his valuable help in using the ESRF beam line and D. P. Datta for his assistance in sample preparation. This work was supported by the DST-DAAD India-Germany Collaborative Program.

¹U. Valbusa, C. Boragno, and F. B. de Mongeot, *J. Phys.: Condens. Matter* **14**, 8153 (2002).

²J. Kim, B. Kahng, and A. L. Barabasi, *Appl. Phys. Lett.* **81**, 3654 (2002); M. A. Makeev and A. L. Barabasi, *ibid.* **71**, 2800 (1997).

³T. K. Chini, M. K. Sanyal, and S. R. Bhattacharyya, *Phys. Rev. B* **66**, 153404 (2002).

⁴T. K. Chini, D. Datta, S. R. Bhattacharyya, and M. K. Sanyal, *Appl. Surf. Sci.* **182**, 313 (2001).

⁵M. Nastasi, J. W. Mayer, and J. K. Hirvonen, *Ion-Solid Interactions: Fundamentals and Applications* (Cambridge University Press, New York, 1996).

⁶C. C. Umbach, R. L. Headrick, and K. C. Chang, *Phys. Rev. Lett.* **87**, 246104 (2001).

⁷T. K. Chini, F. Okuyama, M. Tanemura, and K. Nordlund, *Phys. Rev. B* **67**, 205403 (2003).

⁸M. K. Sanyal, A. Datta, and S. Hazra, *Pure Appl. Chem.* **74**, 1553 (2002).

⁹A. Gibaud and S. Hazra, *Curr. Sci.* **78**, 1467 (2000).

¹⁰*X-ray and Neutron Reflectivity: Principles and Applications*, ed-

ited by J. Daillant and A. Gibaud (Springer, Paris, 1999).

¹¹I. K. Robinson and D. J. Tweet, *Rep. Prog. Phys.* **55**, 599 (1992).

¹²H. Dosch, *Critical Phenomena at Surfaces and Interfaces*, Springer Tracts in Modern Physics, Vol. 149 (Springer-Verlag, Berlin, 1992).

¹³V. Holy, U. Pietsch, and T. Baumbach, *High Resolution X-ray Scattering from Thin Films and Multilayers*, Springer Tracts in Modern Physics, Vol. 149 (Springer-Verlag, Berlin, 1999); J. Grenzer, N. Darowski, U. Pietsch, A. Daniel, S. Renon, J. P. Reithmaier, and A. Forchel, *Appl. Phys. Lett.* **77**, 4277 (2000).

¹⁴U. Pietsch, *Curr. Sci.* **78**, 1484 (2000).

¹⁵A. Ulyanekov, N. Darowski, J. Grenzer, U. Pietsch, K. H. Wang, and A. Forchel, *Phys. Rev. B* **60**, 16701 (1999).

¹⁶U. Pietsch, T. H. Metzger, S. Rugel, B. Jenichen, and I. K. Robinson, *J. Appl. Phys.* **74**, 2381 (1993).

¹⁷J. K. Basu, S. Hazra, and M. K. Sanyal, *Phys. Rev. Lett.* **82**, 4675 (1999).

¹⁸G. H. Vineyard, *Phys. Rev. B* **26**, 4146 (1982).

¹⁹<http://www.srim.org/>